Applied Surface Science 631 (2023) 157507

Contents lists available at ScienceDirect

Applied Surface Science

journal homepage: www.elsevier.com/locate/apsusc

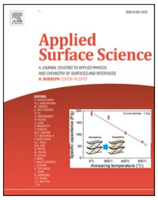

Full Length Article

Rapid laser-induced low temperature crystallization of thermochromic VO_2 sol-gel thin films

Maria Basso [a,b], Elena Colusso [a], Chiara Carraro [c], Curran Kalha [b], Aysha A. Riaz [b], Giada Bombardelli [a], Enrico Napolitani [c], Yu Chen [d], Jacek Jasieniak [e], Laura E. Ratcliff [f], Pardeep K. Thakur [g], Tien-Lin Lee [g], Anna Regoutz [b], Alessandro Martucci [a,*]

[a] Department of Industrial Engineering, University of Padova and INSTM, Via Marzolo 9, Padova 35131, Italy
[b] Department of Chemistry, University College London, 20 Gordon Street, London WC1H 0AJ, United Kingdom
[c] Department of Physics and Astronomy and LNL-INFN, University of Padova, Via Marzolo 8, Padova 35131, Italy
[d] Monash Centre for Electron Microscopy (MCEM), Monash University, Clayton, Victoria 3800, Australia
[e] Department of Materials Science and Engineering, Monash University, Clayton, Victoria 3800, Australia
[f] Centre for Computational Chemistry, School of Chemistry, University of Bristol, Bristol BS8 1TS, United Kingdom
[g] Diamond Light Source Ltd, Harwell Science and Innovation Campus, Didcot, Oxfordshire OX11 0DE, United Kingdom

ARTICLE INFO

Keywords:
Vanadium oxide
Sol gel
Laser
Thermochromic
Smart windows
Photonic curing

ABSTRACT

The thermochromic properties of vanadium dioxide (VO_2) offer great advantages for energy-saving smart windows, memory devices, and transistors. However, the crystallization of solution-based thin films at temperatures lower than 400°C remains a challenge. Photonic annealing has recently been exploited to crystallize metal oxides, with minimal thermal damage to the substrate and reduced manufacturing time. Here, VO_2 thin films, obtained via a green sol–gel process, were crystallized by pulsed excimer laser annealing. The influence of increasing laser fluence and pulse number on the film properties was systematically studied through optical, structural, morphological, and chemical characterizations. From temperature profile simulations, the temperature rise was confirmed to be confined within the film during the laser pulses, with negligible substrate heating. Threshold laser parameters to induce VO_2 crystallization without surface melting were found. With respect to furnace annealing, both the crystallization temperature and the annealing time were substantially reduced, with VO_2 crystallization being achieved within only 60 s of laser exposure. The laser processing was performed at room temperature in air, without the need of a controlled atmosphere. The thermochromic properties of the lasered thin films were comparable with the reference furnace-treated samples.

1. Introduction

The efficient production of energy through green and low-impact approaches is a fundamental challenge of this century, since the increasing energy demand needs to be satisfied while simultaneously minimizing greenhouse gas emissions. As buildings' fenestration and heating, ventilation and conditioning systems are currently responsible for 30–40% of the world's energy consumption, [1] energy-saving devices have been proposed to reduce the energy misuse, with a particular focus on smart windows and chromogenic coatings. The optical properties of the latter can be manipulated via external stimuli such as applied voltage, gas involving reactions, or environmental temperature, which dictate the overall behavior of electro-, gaso- and thermochromic materials, respectively. Electro- and gasochromic materials offer promising performance for these applications, however, it remains challenging to apply them in large-scale manufacturing due to long-term instability resulting in limited switching cycles [2].

Thermochromic coatings are the most investigated chromogenic materials, among which vanadium dioxide (VO_2) has emerged for its outstanding properties. VO_2 offers passive control of the transmitted sunlight, since drastic changes of its optical transmission in the near infrared (NIR) can be induced by environmental temperature oscillations above and below a specific critical temperature (T_c) [1]. Correspondingly, the coating's electrical resistivity manifests variations up to four orders of magnitude as a function of the external temperature [3]. This temperature dependence of optical and electrical properties

---

* Corresponding author.
E-mail address: alex.martucci@unipd.it (A. Martucci).

https://doi.org/10.1016/j.apsusc.2023.157507
Received 17 March 2023; Received in revised form 3 May 2023; Accepted 10 May 2023
Available online 13 May 2023
0169-4332/© 2023 The Authors. Published by Elsevier B.V. This is an open access article under the CC BY license (http://creativecommons.org/licenses/by/4.0/).

provides a clear path to reduce the reliance on fossil fuels, without the need for active inputs such as voltage or gaseous components. Nonetheless, if an active control is preferred, pressure, strain or electrostatic fields can also be used to trigger the optical and electrical switching of VO_2 [4]. The underlying mechanism causing the switching is attributed to a concurrent structural and electrical transition. At room temperature, VO_2 exhibits a monoclinic crystalline structure, which allows the transmission of NIR wavelengths coupled with semiconducting behavior. Above its T_c, the atoms rearrange into a tetragonal rutile structure, leading to reflection of the NIR frequencies and metal-like behavior. The metal–insulator transition (MIT) of pure VO_2 occurs at 68°C, but the T_c can be increased or decreased by doping or by introducing strain, defects, or non-stoichiometry in the crystal structure [5–7]. The lattice and electronic switch to the metallic phase involves disordering of vanadium dimerized pairs and band collapsing at the femtosecond scale. Tens to hundreds of picoseconds are then needed for the rutile metallic phase to locally nucleate and grow [8,9].

VO_2 films and coatings have been conventionally deposited through sputtering, chemical and physical vapor deposition. These require complex and expensive equipment and can be time-consuming [6]. Solution-based methods are based on simple and straightforward processes, which can offer precise control of coating properties, lower cost, and scalability over large-area substrates [10].

Generally, as-deposited solution-processed metal oxide (MO) coatings are amorphous and require thermal treatments to obtain a crystalline structure. This is achievable only for substrates that can withstand the high temperatures (i.e., above ~400°C) required by the crystallization process, which therefore excludes polymers and low melting temperature metals. Alternative solutions, such as the incorporation of previously crystallized nanoparticles in polymeric matrices, are more sensitive to the environment and cannot achieve uniform optical or electrical performance, due to low connectivity between individual particles [1]. The successful crystallization of uniform metal oxide coatings on temperature-sensitive substrates would make a wide range of innovative solutions available to tackle the increasing worldwide energy demand. Unconventional techniques, such as photonic curing, have gained attention for the development of actuators, memory-devices, transistors and flexible electronics, based on VO_2 or other MOs [1,11]. Photons of appropriate wavelengths are used to induce localized photothermal and/or photochemical effects in the coating, avoiding thermal damage of the underlying substrate. The three main types of photonic curing, namely deep ultraviolet (DUV) irradiation, lasers, and flash lamps, substantially differ in terms of temporal and spatial energy distribution inside the film, process timescale, and irradiation range [12–14]. Among them, laser annealing is a particularly promising alternative to conventional thermal treatments, offering accurate control of the energy distribution inside the coatings in both space and time.

The extremely fast laser processing allows reduced manufacturing time, roll-to-roll versatility, and scalability over large substrate areas [12,15,16]. Currently, few studies exploit photonic annealing to crystallize metal oxides at temperatures lower than 400°C [14,17]. Considering VO_2, Jo *et al.* decreased the crystallization temperature of sol–gel coatings by combining deep ultraviolet (DUV) irradiation and combustion, while Nishikawa *et al.* laser-treated metal–organic deposited films [18,19]. Other groups used UV lasers as post-crystallization treatments, to improve the electrical connectivity between particles, to change from diamagnetic to ferromagnetic behavior, or to modify the morphology and color of crystalline films [20–22].

In the present work, vanadium oxide thin films were deposited through a green sol–gel synthesis, based on a non-toxic precursor and solvent without supplementary additives. The films' densification and crystallization to VO_2 was achieved by excimer laser irradiation. In contrast to conventional thermal treatments, which require inert atmospheres to avoid the formation of other vanadium oxides [6], the laser treatment was performed in air. Since the influence of laser energy density and number of pulses on VO_2 films is not yet fully understood, the two parameters were systematically varied to gain in-depth knowledge of their effect. The threshold values for laser-induced crystallization of VO_2 were found for silicon and fused silica substrates. Crystallization was reached within 1 min, in contrast with time- and energy- consuming thermal annealing in a furnace. The influence of laser parameters and substrate type on the films' optical, chemical, and morphological properties were explored through several techniques, including X-ray diffraction (XRD), soft and hard X-ray photoelectron spectroscopy (SXPS, HAXPES), transmission and scanning electron microscopy (TEM, SEM), and UV–Vis-NIR spectroscopy.

2. Materials and methods

2.1. VO_2 thin film synthesis and deposition

Silicon wafers (P-type, ⟨1 0 0⟩, single-side polished, Silicon Materials) and fused silica substrates (Quartz, Electro optical technology) were rinsed in absolute ethanol (EtOH, 99.9%, Emsure, Sigma Aldrich, UK) and dried with nitrogen. Residual organic contaminants were removed by atmospheric plasma cleaning (Plasma Cleaner, PDC-002-CE, Harrick Plasma, USA). The starting solution, adapted from Pan *et al.* [23], was prepared by dissolving vanadyl acetylacetonate powder ($VO(acac)_2$, 98%, Sigma-Aldrich) in absolute ethanol in a 0.125 M concentration. The solution was stirred at 85°C in a round-bottom flask under reflux for 9 h, after which it was aged for 15 h at room temperature. Subsequently, the solution was filtered with 0.2 μm sized syringe filters and spin coated on the pre-cleaned substrates at 2000 rpm for 30 s. Only for drying temperature tests, the films were deposited by dip coating at 300 mm/min. Samples were coated from 1 to 3 layers to tune the thickness of the film. Each layer was dried at 85 °C on a hot plate for 15 min prior to the deposition of the following one. After the deposition, the films were dried on a hot plate in air for 10 min, at temperatures ranging between 80 and 300°C.

2.2. Densification and crystallization by laser and furnace annealing

The dried films were laser-annealed one day after the deposition. A KrF excimer laser system (248 nm, Coherent COMPex 201F, 22 ns pulse duration) was used to irradiate the samples in distinct and isolated parts of the total surface. Each spot had a 5 × 5 mm^2 size, with uniformity of 2%. The irradiation was carried out in air at room temperature with a variable number of pulses (#), at fixed repetition rate of 10 Hz with a laser fluence between 40 and 700 mJ/cm^2 for the initial energy density scan and 40–200 mJ/cm^2 for the following tests. Fluence was controlled through a motorized attenuator paired with an in-line energy meter, with an accuracy of 1%. Reference samples were annealed in a tube furnace at 550°C for 1 h, with a heating ramp of 10°C/min in a nitrogen environment.

2.3. Characterization

Thickness, refractive index (n), and extinction coefficient (k) of the films were obtained with a J.A. Woollam Co. spectroscopic ellipsometer (Woollam M2000) across 300–1200 nm at incident angles of 65°–70°–75° for silicon wafers and 50°–60°–70° for fused silica. The materials were modeled using GenOsc models with Tauc-Lorentz, Lorentz, and/or Drude oscillators. On the silicon substrates, the absorption coefficient (α) was calculated from Equation (1):

$$\alpha = \frac{4\pi k_\lambda}{\lambda} \tag{1}$$

in which k_λ is the extinction coefficient and λ is the laser wavelength ($\lambda = 248$ nm). The penetration depth (δ) of the laser radiation can be calculated as the inverse of the absorption coefficient ($\delta = 1/\alpha$). The extinction coefficients at 248 nm were generated from the ellipsometric fittings. The estimated penetration depths are reported in Table S2 in the Supporting Information (SI). The transmittance spectra were collected with a UV–Vis-NIR spectrophotometer (Jasco V770), at 200 nm/min in the wavelength range 190–2500 nm. The transmittance was collected both at 20°C and 90°C with the aid of a custom-made heating cell attachment. The transition temperature (T_c) was calculated as the mean value between the transition temperature during heating (T_{heat}) and the transition temperature during cooling (T_{cool}). The T_{heat} and T_{cool} were obtained from the first derivative of the transmittance respect to the temperature during the heating and cooling cycles, respectively. The luminous transmittance (T_{lum}) and the solar modulation ability (ΔT_{sol} and $\Delta T_{2000\ nm}$) were used to evaluate the thermochromic performance [24]. The integrated luminous transmittance (T_{lum}) was obtained by Eq. (2):

$$T_{lum} = \frac{\int \varnothing_{lum}(\lambda)T(\lambda)d(\lambda)}{\int \varnothing_{lum}(\lambda)d(\lambda)} \tag{2}$$

in which $\varnothing_{lum}$ represents the photonic vision luminous efficiency function and T_λ represents the transmittance at wavelength λ. The standard integration range for luminous transmittance is 380 to 780 nm. The solar modulation ability (ΔT_{sol}) was obtained by Equation (3):

$$\Delta T_{sol} = T_{sol,lt} - T_{sol,ht} \tag{3}$$

in which $T_{sol,lt}$ is the solar transmittance at low temperature (i.e., semiconducting state – 20°C) and $T_{sol,ht}$ is the solar transmittance at high temperature (i.e., metallic state – 90°C). The solar transmittance (T_{sol}) was calculated as Equation (4):

$$T_{sol} = \frac{\int \varnothing_{sol}(\lambda)T(\lambda)d(\lambda)}{\int \varnothing_{sol}(\lambda)d(\lambda)} \tag{4}$$

where $\varnothing_{sol}$ is the standard solar radiation spectrum for the air mass 1.5 (AM 1.5) and the standard integration range is 250 to 2500 nm. Finally, the solar modulation ability at a fixed wavelength of 2000 nm was calculated by $\Delta T_{2000\ nm} = T_{20^\circ C} - T_{90^\circ C}$.

The crystal structure of the films was characterized with glancing angle X-ray diffraction (XRD) on a Philips PW1710 diffractometer equipped with a grazing incidence Cu Kα X-ray source ($\lambda = 1.5406$ Å). The silicon substrate contribution at ~34° was cut from the graphs to exclude the substrate influence. The Scherrer equation $D = K\lambda/(w\cos\theta)$ was used to estimate the average crystallite size (D), with $K = 0.94$, $\lambda = 0.15406$ nm X-ray wavelength, θ the Bragg angle, and w the full width at half maximum of the latter Bragg angle. Raman spectra were collected using a Renishaw inVia Raman Microscope with a 633 nm He:Ne laser, with three iterations of 30 s accumulation time in the range 100–540 cm^{-1} and 540–1000 cm^{-1} to exclude the signal from the silicon substrate.

The surface morphology of the samples was investigated by scanning electron microscopy (FE-SEM, Zeiss). The cross-section of the films was prepared using the Thermo Scientific Helios 5 UX FIB-SEM. Deposition of Carbon and Platinum were applied to protect the surface. The elemental distribution was studied by the FEI Tecnai G2 F20 S-TWIN transmission electron microscopy (TEM) with the Bruker X-ray detector.

Chemical analysis using laboratory-based soft X-ray photoelectron spectroscopy (SXPS) was performed on a Thermo Scientific K-Alpha X-ray photoelectron spectrometer, with a 2×10^{-9} mbar base pressure. A monochromated Al Kα was used as the X-ray source ($h\nu = 1486.7$ eV, further referred to as 1.5 keV for simplicity). Survey and key core level spectra were collected using 200 eV and 20 eV pass energy, respectively, with a 400 μm spot size. A flood gun was used to minimize sample charging. Synchrotron-based hard X-ray photoelectron spectroscopy (HAXPES) was performed at beamline I09 at the Diamond Light Source, UK, using an X-ray photon energy of 5927.4 eV (further referred to as 5.9 keV for simplicity). The analysis chamber of the beamline end station has a base pressure of ~3.5×10^{-10} mbar and measurements were performed in grazing incidence and near normal emission geometry to allow efficient spectra collection. Survey and core level spectra were collected using a pass energy of 200 eV. For both SXPS and HAXPES, the binding energy (BE) scale of all spectra was aligned to the adventitious carbon peak in the C 1*s* spectra at a binding energy (BE) of 284.8 eV (determined from peak-fit analysis). The spectra were normalized to the total V $2p_{3/2}$ spectral area, after the removal of a Shirley-type background. The Avantage software package was used to analyze the data. The QUASES software package was used to estimate the maximum inelastic mean free path (λ_{IMFP}) for bulk VO_2, with values of ~3 nm at 1.5 keV (SXPS) and ~9 nm at 5.9 keV (HAXPES) [25]. The total probing depth can be estimated as 95% of the signal intensity (i.e. $3\lambda_{IMFP}$), giving values of ~9 nm and ~27 nm for SXPS and HAXPES, respectively.

Simulations of the temperature profiles and their evolution during laser processing were produced as a function of both depth (i.e. film thickness) and laser irradiation time. Numerical solutions of the heat equation based on heat flow calculations were performed by employing the LIMP software (Harvard simulation software package) [26] and calibrated on VO_2 and fused silica physical and optical data. The former were chosen from the literature [27,28], whereas the latter were calculated from experimental data obtained in this work. The absorption coefficient (α) was calculated from the equation $\alpha = (A\lambda)/t$, in which λ is the laser wavelength ($\lambda = 248$ nm). The penetration depth (δ) of laser radiation can be calculated as the inverse of the absorption coefficient ($\delta = 1/\alpha$).

3. Density functional theory calculations

To corroborate peak analysis in SXPS and HAXPES, core BE calculations were performed to estimate the relative BE distance between O and C atoms in the precursor structure. Calculations were performed using density functional theory (DFT) [29,30], using the CASTEP plane wave DFT code [31]. The PBE exchange–correlation functional [32] was used alongside norm-conserving pseudopotentials with 13 valence electrons for V, a kinetic energy cut-off of 1200 eV (1000 eV) for the geometry optimization (core BE calculations) and a Monkhorst-Pack [33] *k*-point grid of 2 × 2 × 1. The geometry optimization employed the empirical dispersion correction scheme of Tkatchenko-Scheffler [34], while both the atomic positions and unit cell were allowed to relax. Relative core BEs were then calculated for the relaxed structure, using the ΔSCF approach with on-the-fly generated core hole PSPs. The core BE calculations were performed using spin polarization; this was found to have little impact on the geometry optimization, and so was neglected in the latter case.

4. Results and discussion

A general process overview for the laser-induced crystallization of sol–gel VO_2 thin films is reported in Fig. 1. Following the synthesis and deposition steps (see Experimental section for detailed procedure), the thin films were dried at low temperature and photonically treated with a KrF excimer laser. The evolution of the sol–gel films during laser annealing was studied on silicon and fused silica substrates, exploiting different combinations of laser fluence (i.e., energy density) and number of pulses.

4.1. Low temperature drying

As reported by Yarali *et al.* [12], the initial film quality is expected to have a substantial influence on the final properties and application of the photonically-cured material. Past research on similar sol–gel films has evidenced the need of a low-temperature treatment prior to or during the photonic curing, with minimum temperatures of 250–300°C [18]. This step helps to reach a proper film densification and adhesion to

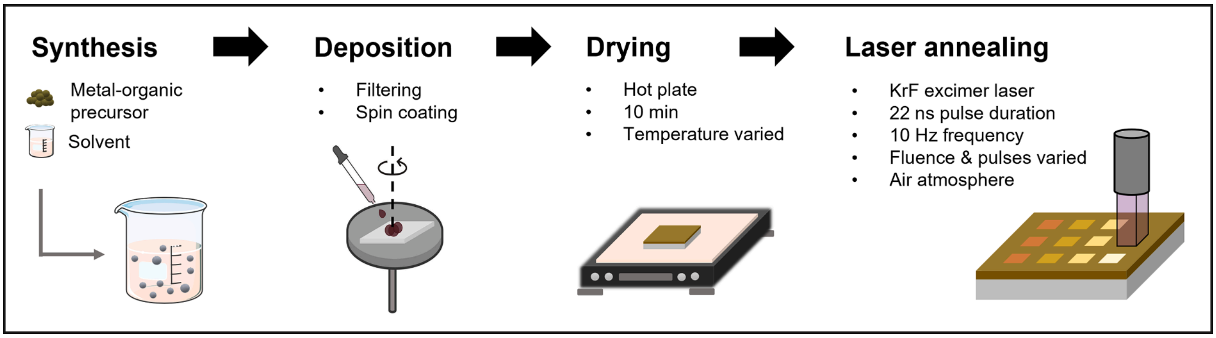

Fig. 1. Schematics of sol–gel VO_2 thin films preparation, including the following stages from left to right: synthesis, deposition, drying and laser annealing.

the substrate, avoiding the film ablation observed upon direct exposure to laser light [35]. Here, the drying temperature was studied to promote sol–gel condensation and impurity removal, with the goal of simultaneously avoiding film ablation and uncontrolled crystallization. Single-layer films were deposited on silicon substrates and XPS was used to compare four different drying temperatures, in the 80–300°C range. The lowest value was chosen just above the boiling point of the solvent (~78°C) to allow for a gentle evaporation [36]. The highest value was chosen to strongly promote film condensation and densification along with removal of organic components. These temperatures are lower than those used in conventional thermal treatments of similar solution-based films, where the minimum reported temperature for VO_2 crystallization is 440–550°C [2,23,37].

The core level spectra for the dried samples are shown in Fig. 2 (a)-(b) and in Fig. S1 (a) in SI. The three main features visible in the C 1*s* core levels are assigned to adventitious carbon and C—C/C—H environments (284.8 eV), O—C—O (~286.6 eV) and O—C═O (~288.6 eV) environments, respectively [38]. With increasing drying temperature, the overall intensity of the C 1*s* spectra decreases relative to the V $2p_{3/2}$ spectral area. This can be explained by the release of acetylacetone (Hacac) during the oxidation of $VO(acac)_2$ in alcohol, as previously observed by Gryboś *et al.* [39]. The removal of Hacac during drying is favored at temperatures between 150 and 200°C, which are above the boiling point of acetylacetone (~140°C) [40]. At the highest drying temperatures, the thermal decomposition of residual metal precursor, which was found to start at ~220°C, may also contribute to the reduction observed in the *C* signal intensity [41,42].

Alongside the observed changes in the C 1*s* core level, the O 1*s* core level was used to monitor the changes in the oxygen chemical state, namely the metal-oxide conversion and the hydroxyl contribution. From peak fit analysis and theoretical calculations (see Fig. S1 (b-c) and Fig. S2 in SI), two main features were attributed to V—O—H (~531.7 eV) and V—O—V (~530.5 eV) environments, alongside with a smaller contribution from organic C—O/C═O environments (~533 eV) [14,38,43]. The presence of hydroxylated V—OH groups, which is strongly evident in the drop-cast solution and in the film dried at 80°C, decreases when the drying temperature is higher than 150°C. This goes hand-in-hand with a decrease in the V—O—H:V—O—V ratio, which highlights the progress of condensation reactions and the development of V—O—V networks.

Additional characterizations were performed to investigate eventual changes in thickness and structural properties. Ellipsometry measurements showed a moderate film densification from 80 to 300°C, with a ~13% decrease in thickness (see Table S1 in SI). XRD was performed on the 300°C dried sample, which displayed amorphous characteristics with no detectable diffraction peaks (Fig. 4 (a)). Interestingly, the TEM analysis (Fig. 2 (c-d)) evidenced the presence of small crystallites in the overall amorphous matrix. These crystallization seeds were only ~1-2 nm in dimension and could not be detected by XRD.

Based on the previous results, a drying temperature of 300°C was selected for all further sample preparation as it allows for the best removal of impurities, provides good film densification, and avoids direct ablation before the laser-induced crystallization.

4.2. *Laser-thin film interaction*

Following the exploration of the appropriate film drying temperature, the interaction between sol–gel coating and UV laser setup was investigated for silicon substrates. The exhaustive review by Yarali *et al.* examined the complexity of laser-matter interaction in detail [12]. Numerous principal factors contribute to this, including pulse number, laser fluence, and energy density profile of the laser, as well as optical path, absorption coefficient, morphology, and thermal conductivity of the film material, which influence how the laser energy is distributed inside the film. Additionally, the complexity of the sol–gel process itself, which typically involves hydrolysis and condensation reactions as well

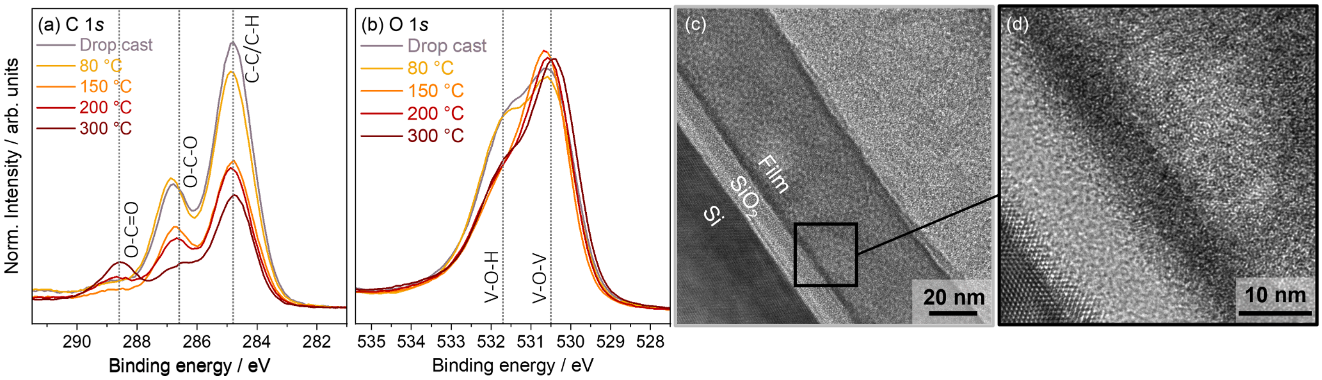

Fig. 2. Key core level XP spectra of the drop cast solution and of the samples dried using temperatures from 80 to 300°C, including (a) C 1*s* and (b) O 1*s*. The reference lines represent the position of the main identified spectral features. (c-d) TEM cross-sections of the dried thin film at 300°C. The relative scale bars are inserted at the bottom of each image.

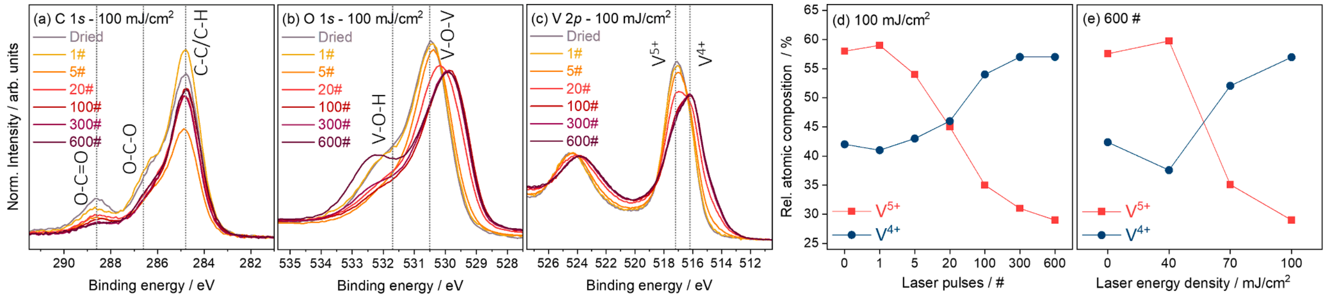

Fig. 3. XP spectra of laser annealed thin films at 100 mJ/cm^2 with varying pulse numbers, including (a)-(c) C 1*s*, O 1*s* and V 2p core level spectra. The reference lines represent the position of the main identified spectral features. V^{4+} and V^{5+} oxidation state populations from peak fit analysis of the V $2p_{3/2}$ core level spectra, for (d) films treated at 100 mJ/cm^2 with varying pulse numbers and for (e) films treated with 600 laser pulses at varying laser fluence, respectively.

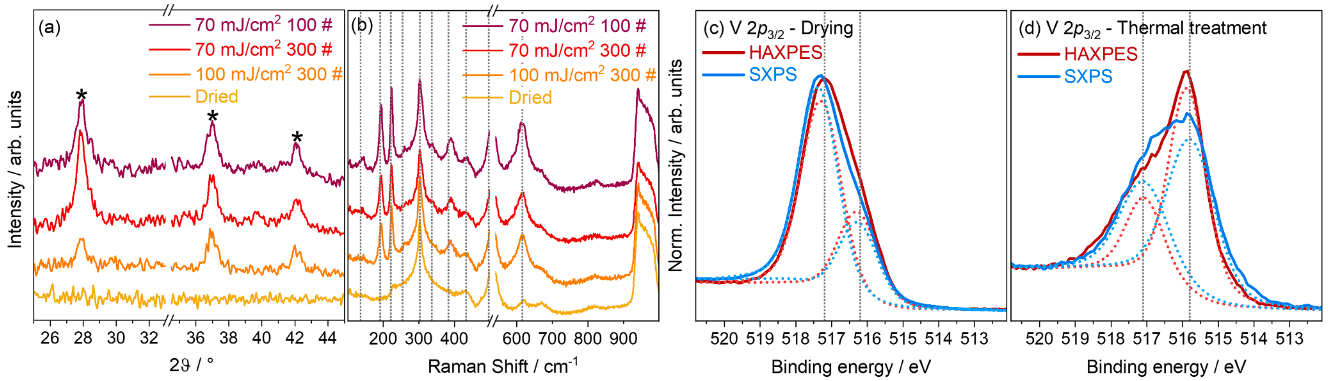

Fig. 4. (a) XRD pattern and (b) Raman spectra of the dried film and of the lasered spots, at laser parameters of 70 mJ/cm^2 100–300 # and 100 mJ/cm^2 300 #. The reference symbols and lines in (a) and (b) represent the VO_2 XRD pattern and Raman spectral profile, respectively. (c) SXPS and (d) HAXPES collected V $2p_{3/2}$ core level spectra of the dried film and of the furnace treated film, respectively.

as interactions with additives, further increases the challenges of understanding the mechanism of laser-matter interactions [44].

Based on existing studies of KrF laser-treated sol–gel films [12,43,45–47], the first sample set in the present study was prepared by exposing a dried film to single ns laser pulses (#) of increasing laser fluence, which was varied in the range of 30–700 mJ/cm^2. The initial film thickness (*t*) was determined using ellipsometry and found to be 33 ± 3 nm. Each single-pulse lasered spot had an area of 5 × 5 mm^2 and a separation of 5 mm from the next laser spot to exclude the influence of thermal diffusion. The edges and inner surface of the lasered spots were analyzed with a profilometer (see Fig. S3 in SI). A single pulse in the fluence range of 30 to 80 mJ/cm^2 led to an increase in surface roughness with unclear boundaries around the irradiated area. The edges became more defined above 100 mJ/cm^2. Above 600 mJ/cm^2 the step height at the edge of the lasered area matched the film thickness (i.e., 33 nm), indicating that a complete ablation of the film material occurred. Therefore, on the subsequent sample set the laser fluence was varied between 40 and 200 mJ/cm^2, to investigate the influence of consecutive pulses and simultaneously reduce the thermal load of a single pulse. The reduction of the energy density is beneficial for the ultimate goal of extending metal oxide densification and crystallization on polymeric substrates.

Following the findings for single pulses, the influence of increasing pulse number and fluence was separately studied using XPS. Two identical thin films with t = 21 ± 2 nm were deposited on 5 × 5 cm^2 silicon substrates. To study the influence of the number of pulses, six spots were lasered at a fixed energy density of 100 mJ/cm^2 with pulse numbers of 1, 5, 20, 100, 300 and 600. The C 1*s*, O 1*s* and V 2*p* core levels, shown in Fig. 3 (a-c), were used to monitor the chemical variations of the films. As expected, the C 1*s* features (Fig. 3 (a)) decreased in intensity with increasing pulse number. In both the O 1*s* and V 2*p* spectra (see Fig. 3 (b-c)) continuous changes up to 100 pulses were visible, which stabilized thereafter. In the O 1*s* core level, the main lowest BE feature between 529.5 and 530.5 eV is related to the O^{2-} ions of the amorphous or crystalline metal–oxygen network [48], and the second feature at a BE of ~531.7 eV arises from hydroxyl groups. No clear trend could be observed between the lower BE oxide feature and the hydroxyl peak as the latter depends on a range of surface-related factors (including surface chemistry and roughness), which all change in a complex fashion when the number of laser pulses changes. The highest BE feature at ~533.5 eV, which intensity increased with increasing pulses, can be related to the native oxide layer covering the substrate [49]. The increasing pulses probably led to a reduction of film's thickness, which allowed to partially probe the silica layer below the film. A systematic shift to lower BE of the lowest BE feature is observed with increasing pulse number with a maximum BE difference of ~0.4 eV. This variation can arise from an interplay between changes in (i) the chemical environment due to differences in V-O-V network development, (ii) the V oxidation state, and (iii) the amorphous-to-crystalline structural changes. Similar shifts in O 1*s* BE were seen in other studies [50,51].

The V 2*p* core level spectra also showed systematic changes with increasing number of pulses (Fig. 3 (c)). They are dominated by two features at ~517.2 eV and ~516.1 eV, stemming from V^{5+} and V^{4+}, respectively. A smaller shoulder at ~514.5 eV arising after higher pulse numbers is attributed to V^{3+} [37,52,53]. From peak fit analysis of the V 2*p* spectra the contributions of the V^{5+} and V^{4+} states could be quantified and are shown in Fig. 3 (d). Before laser curing, the oxidized V^{5+} state was predominant in the film with a ~60% contribution. A single pulse at 100 mJ/cm^2 did not lead to significant changes, whereas with increasing pulse exposure, the population of V^{5+} decreases in favor of V^{4+}. The contribution from V^{3+} was below 10% for all samples. Above 300 pulses the V^{4+} contribution reaches a maximum at ~60%. Bordelet *et al.* [54] speculated that the reduction to V^{4+} could be favored by the decomposition of residual organic species inside the film. Considering the Ellingham diagram, VO_2 crystallization is not expected at room temperature in air but could be expected at lower oxygen partial pressures (pO_2) [55,56]. Even if the 10 min drying treatment at 300°C favored a decrease in carbon content, a residual organic component was expected due to the short time and low temperature of drying as confirmed in the XPS spectra (Fig. 2 (a)). The increasing pulse numbers led to a progressive reduction in the carbon content (Fig. 3 (a)), which was concurrent with the progressive increase in the V^{4+}/V^{5+} ratio (Fig. 3 (c)). This could be evidence that the mechanism suggested by Bordelet *et al.* applies in the present case.

The influence of energy density was also explored by applying a fixed pulse number of 600 and laser-curing three spots at 40, 70, and 100 mJ/cm^2, respectively. All three XPS core levels (see Fig. S4 (a-c) in SI) presented the same features described for the pulse effect. With respect to the 100 mJ/cm^2 treated sample, a lower fluence of 40 or 70 mJ/cm^2 did not lead to higher organic residuals in the C 1*s* spectra. This can be related to the high number of pulses, which was effective in reducing the organic content even at lower energy densities. The V 2*p* spectra were again peak fitted to evaluate the contribution of each oxidation state (Fig. 3 (e)). Compared to the non-lasered film, the V^{5+}/V^{4+} ratio did not vary significantly at 40 mJ/cm^2, with V^{5+} being predominant (~60%). In contrast at fluences of 70 and 100 mJ/cm^2 a clear increase in V^{4+} contribution is observed.

In literature, the main accepted mechanism for the densification or crystallization during photonic curing is attributed to photochemical and/or photothermal processes. The selective and extremely fast laser irradiation induces a localized heat over a nanosecond timescale, only partially involving the superficial layers of the substrate without affecting the bulk. Respect to a continuous laser, a pulsed laser irradiation allows to control the heat distribution inside the film, since the short timescales and large temperature gradients do not induce high energy transfers to the surrounding areas. This leads to a great reduction of the heat-affected zones, both laterally and in-depth. Respect to UV lamps, which lead to continuous annealing times within seconds to minutes, the pulsed laser annealing is performed over 1–1000 ns. The heating rates differ by orders of magnitude, from 10-10^3 K/s for halogen lamps to $> 10^8$ K/s for pulsed lasers [57].

Regarding laser annealing, there is no complete agreement whether the underlying mechanism is to be attributed only to photothermal effects or to photochemical reactions as well. According to Yarali *et al.* [12], pulsed lasers induce different effects in function of the pulse duration: nanosecond pulses are mainly responsible for thermal effects, whereas femtosecond pulses can lead to cold ablation of the films. The authors highlight the difference between the two processes: the photothermal effect of ns lasers can trigger chemical reactions and precursor conversions, while photochemical reactions and metal–organic bond breaking can be reached with fs lasers. When sol–gel films are considered, the energy absorbed during the ns laser pulses leads to a local increase of temperature, which aids the conversion to a metal-oxide film.

To better investigate the chemical variations observed with XPS, the lasered area for each combination of fluence-pulses was extended to 1.5 × 1.5 cm^2 to characterize its crystalline structure, phase, and morphological properties. A thin film was deposited on a 5.5 cm^2 silicon wafers with a thickness of 29 ± 2 nm. The film was laser-treated with four combinations of laser fluence and number of pulses, each performed on a separated area of the film. The process parameters were chosen considering the influence of pulse number and fluence previously investigated and selected to be 70 mJ/cm^2 at 100–300 – 600 # and 100 mJ/cm^2 at 300 #. A reference sample was prepared by thermally annealing a film at 550°C in a tubular furnace under a nitrogen atmosphere.

The material structure of the lasered spots was characterized by XRD (Fig. 4 (a) and Fig. S5 (a) in SI) and Raman spectroscopy (Fig. 4 (b)), which both confirmed the successful crystallization into monoclinic VO_2 (M1). To enhance the quality of these characterizations, the lasered spots were reproduced with the same laser parameters on a thicker film (92 ± 3 nm). In the former, the main peak at 27.8° highlighted the formation of a predominant (0 1 1) orientation, while the two smaller peaks at 37.1° and 42.2° corresponded to (2 0 0) and (2 1 0) phases of VO_2 (M1) [58–60]. The reference sample, furnace treated at 550 °C, showed a more pronounced (0 1 1) orientation (Fig. S5(b) in SI). The average crystallite size (~13 nm) did not vary among the samples. Coherently with XRD, the Raman spectra shown in Fig. 4 (b) displayed peaks at 143, 193, 223, 261, 307, 334, 389, 437, 497 and 615 cm^{-1} which commensurate with VO_2 [52,61], whereas the other visible peaks were due to the silicon substrate [62].

Previous studies have shown that a thin oxidized overlayer forms when VO_2 is exposed to air and that a gradual transition to V_2O_5 can be induced in conditions of high relative humidity [63,64]. Here, hard X-ray photoelectron spectroscopy (HAXPES) was employed to probe deeper within the film respect to soft XPS (SXPS), to ascertain a depth distribution profile of the V^{5+} oxidation state (see Experimental Section for probing depth estimations). This was done by comparing the variations in oxidation state by peak fitting the V $2p_{3/2}$ core level. The amorphous dried film was compared to the thermally annealed sample (Fig. 4 (c-d)), on which the presence of bulk VO_2 was previously confirmed by XRD (Fig. S5 (b) in SI). From the photoelectron spectroscopy measurements on the amorphous dried sample, the V^{5+} state was confirmed to be dominant even at deeper probing depths, since the ratio between V^{5+} and V^{4+} did not significantly change with increasing probing depth. The presence of residual V^{4+} state could be due to incomplete oxidation of the precursor during the initial synthesis. On the contrary, the V^{5+} state was seen to decrease on the two crystallized samples when the probing depth was increased by HAXPES. The variations found with increasing probing depth from SXPS to HAXPES to bulk XRD confirmed the superficial nature of the oxidized state.

Following the XRD, Raman, and XPS characterizations, the SEM and TEM analysis is reported in Fig. 5 and Fig. S6 in SI. Fig. S6 (a) shows that the dried film (i.e., before laser-annealing) had a smooth, compact and uniform surface morphology. Fig. 5 (a) shows that 100 pulses at a fluence of 70 mJ/cm^2 induced the formation of a porous surface network, containing nanometer-sized holes. Increasing the pulse number to 300 (Fig. 5 (b)) and 600 (Fig. S6 (b) in SI) gradually transformed the morphology to a closely-packed structure, with fewer and smaller holes inside them. Similar patterns were found after KrF laser irradiation on other metal-oxide sol-gels films.[65,66] When the fluence was increased to 100 mJ/cm^2, while keeping constant the pulse number (300 #, Fig. 5 (c)), more pronounced variations of the surface morphology were obtained.

The STEM and TEM cross-sections (Fig. 5 (e-f)) confirmed the film thickness measured with the ellipsometer (Table T2 in SI) and the successful crystallization induced by the laser irradiation. Moreover, the EDX analysis (Fig. 5 (g)) verified that major inter-diffusion between film and substrate did not occur after laser annealing. The higher fluence of 100 mJ/cm^2 induced the formation of complex-shaped packed agglomerates, which resembled the morphology of the furnace annealed VO_2 but with bigger dimensions (Fig. 5 (d)). The reference sample showed the typical packed nanoparticle morphology of crystalline solution-based VO_2 [67,68].

The difference in nanoparticle dimension and shape can be attributed to the different heat generation and distribution in the film. During conventional furnace annealing, the heat is uniformly and isothermally distributed throughout the film, whereas the heat generated upon laser light absorption follows an adiabatic regime [57]. The amount of heat generated during laser annealing is influenced by the film's absorption [12]. High energy photons are delivered to the material within each 22 ns laser pulse: the extremely rapid heating and cooling cycles experienced by the film do not allow the gradual heat distribution typical of conventional furnace treatments. According to our simulations (see

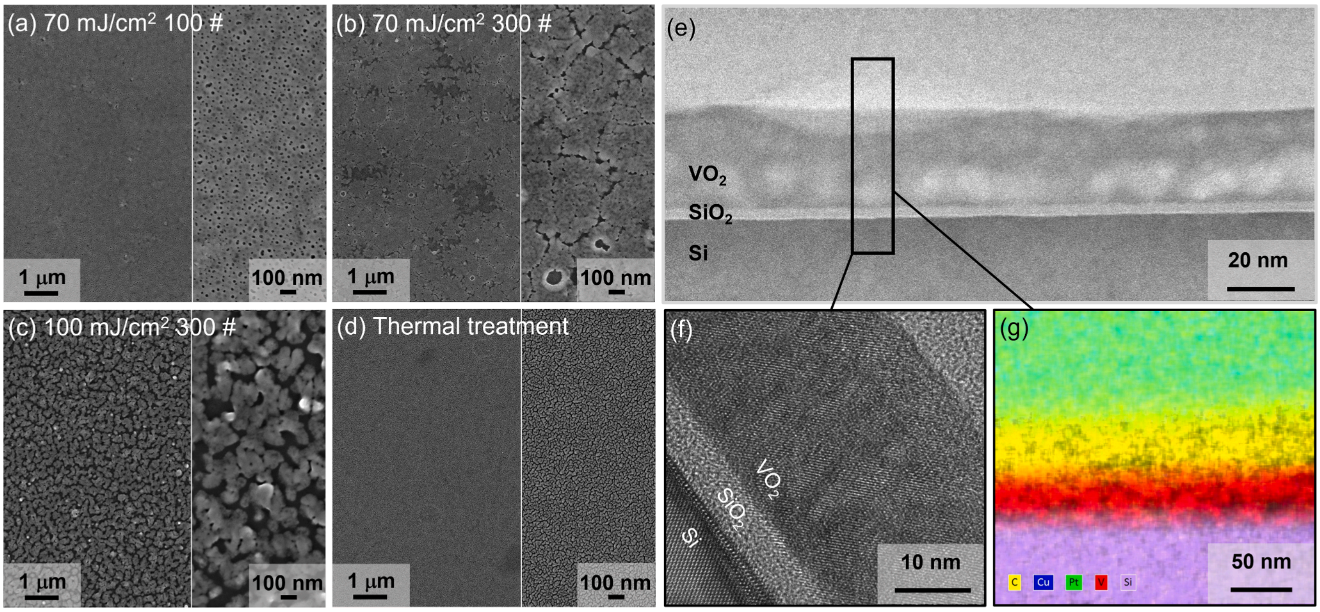

Fig. 5. SEM images of the lasered spots at (a) 70 mJ/cm^2 100 #, (b) 70 mJ/cm^2 300 #, (c) 100 mJ/cm^2 300 #. (d) SEM image of the reference sample thermally treated at 550°C. (e) STEM and (f) TEM cross-section of the lasered spot at 100 mJ/cm^2 300 #. (g) EDX analysis of the lasered spot at 100 mJ/cm^2 300 #. The relative scale bars are inserted at the bottom of each image.

Fig. 6 (d)), which will be thoroughly discussed in the following section, the high temperature experienced by the films during a single pulse is lowered back to room temperature within a few hundreds of nanoseconds. Moreover, temperature gradients are generated between the surface of the film and the interface with the substrate, which enhances the complexity of the spatial and temporal heat distribution.

In conclusion, a synergistic effect of both pulse number and fluence on the film's properties was found. The starting dried film was successfully crystallized into monoclinic VO_2, by using a 70–100 mJ/cm^2 and above 100 pulses. Respect to the pulse number, the fluence had a predominant impact on the final film properties.

4.3. Substrate influence

Another major factor of influence on photonic curing processing is represented by the substrate underlying the film. Depending on the optical penetration of laser radiation through the film, the UV light may penetrate enough to reach the substrate, which can in turn display different interactions with the radiation in function of its optical and thermal properties [35]. Here, fused silica was employed to consider the influence of a lower thermal diffusivity and lower laser light absorption with respect to silicon. The thermal diffusivity of fused silica is ~1.4 mm^2/s, one order of magnitude lower with respect to silicon (~88 mm^2/s). As shown in Fig. S7, the fused silica substrate displayed a ~15% absorption at the laser wavelength (i.e., 248 nm), while the dried vanadium-based film absorbed >70% of the radiation. Following the previous studies on silicon, the effect of both pulse number and fluence was studied on fused silica substrates. Three identical thin films were deposited on 1.5 × 1.5 cm^2 substrates, with a 33 ± 5 nm thickness. The laser parameters were varied among 40–200 mJ/cm^2 and 10–1200 #, to expand the range of interest.

The thermochromic efficiency was studied by monitoring the changes in optical transmittance at 20°C and 90°C, i.e. below and above the T_c. For each sample, the luminous transmittance (T_{lum}) in the 380–770 nm range, the solar modulation ability at 2000 nm ($\Delta T_{2000\ nm}$) and in the 250–2500 nm range (ΔT_{sol}) were calculated as described in the Experimental section. As a general trend in literature, increases of the solar modulation ability are linked to decreases of the luminous transmittance. The latter is usually less than ~40% for films with a high magnitude of ΔT_{sol}. The current challenge is to simultaneously increase both the parameters, to guarantee a high visible transmittance through the windows ($T_{lum} > 60\%$) as well as a robust solar modulation ability ($\Delta T_{sol} > 10\%$) [2,6].

As shown in Fig. 6 (a-e), 100 pulses at 40 mJ/cm^2 were not sufficient to reach a solar transmittance modulation, since no significant variations of the transmittance above the T_c was detected. The increase in pulse number (300 or 600 #) did not lead to different results. A difference in transmittance between 20 and 90°C was instead reached by increasing the fluence to 70 mJ/cm^2. At this fluence, 100 # led to $\Delta T_{2000\ nm} = 15.4\%$ and $\Delta T_{sol} = 2.6\%$, with a luminous transmittance of 79.5%. Similar efficiencies were obtained by increasing the pulse number from 100 # to 600 # (see Fig. 6 (a)). At 100 #, further increasing the fluence to 100 mJ/cm^2 led to a lower thermochromicity respect to 70 mJ/cm^2, whereas a higher pulse number led to an increased solar modulation ($\Delta T_{2000\ nm} = 16.4\%$ and $\Delta T_{sol} = 3.2\%$ at 600 #). Despite the increased solar modulation, the luminous transmittance was stable around 76–80%. A considerable increase in the solar modulation was reached by doubling the pulse number from 600 # to 1200 # at 100 mJ/cm^2, which led to $\Delta T_{sol} = 4.1\%$ and $\Delta T_{2000\ nm} = 28.7\%$ (see Fig. 6 (b)). This lasered sample exhibited a higher thermochromic performance in terms of both T_{lum} and ΔT_{sol} respect to the corresponding reference sample, which was thermally annealed in the furnace at 550°C (see Fig. 6 (e) and Fig. S8 in the SI). The obtained values align well with single-layer VO_2 thin films in the literature and display a particularly high T_{lum}, which is usually compromised when high values of ΔT_{sol} are reached (Table S3) [2]. A common approach to further increase ΔT_{sol} is the combination of VO_2 with other materials (e.g., TiO_2, ZnO, WO_3) in a multilayer configuration [1,2,6]. The T_c of the lasered and furnace-annealed samples is reported in Fig. S12. The T_c of the 70 mJ/cm^2-300# sample was found to be 68°C, while the T_c of the furnace annealed sample was slightly higher (75°C).

To better understand the heat distribution throughout the film and the temporal scale involved, numerical simulations were used to compare the effect of the fluence during a single pulse. Two types of profile were considered, the temporal profiles (Fig. 6 (d)) and the depth ones (Fig. S9 in SI). As visible in the profiles, the material was subjected to a ns-scale temperature gradient of hundreds of degrees Celsius. The temperature rapidly decreased below 300°C within ~300 ns. The

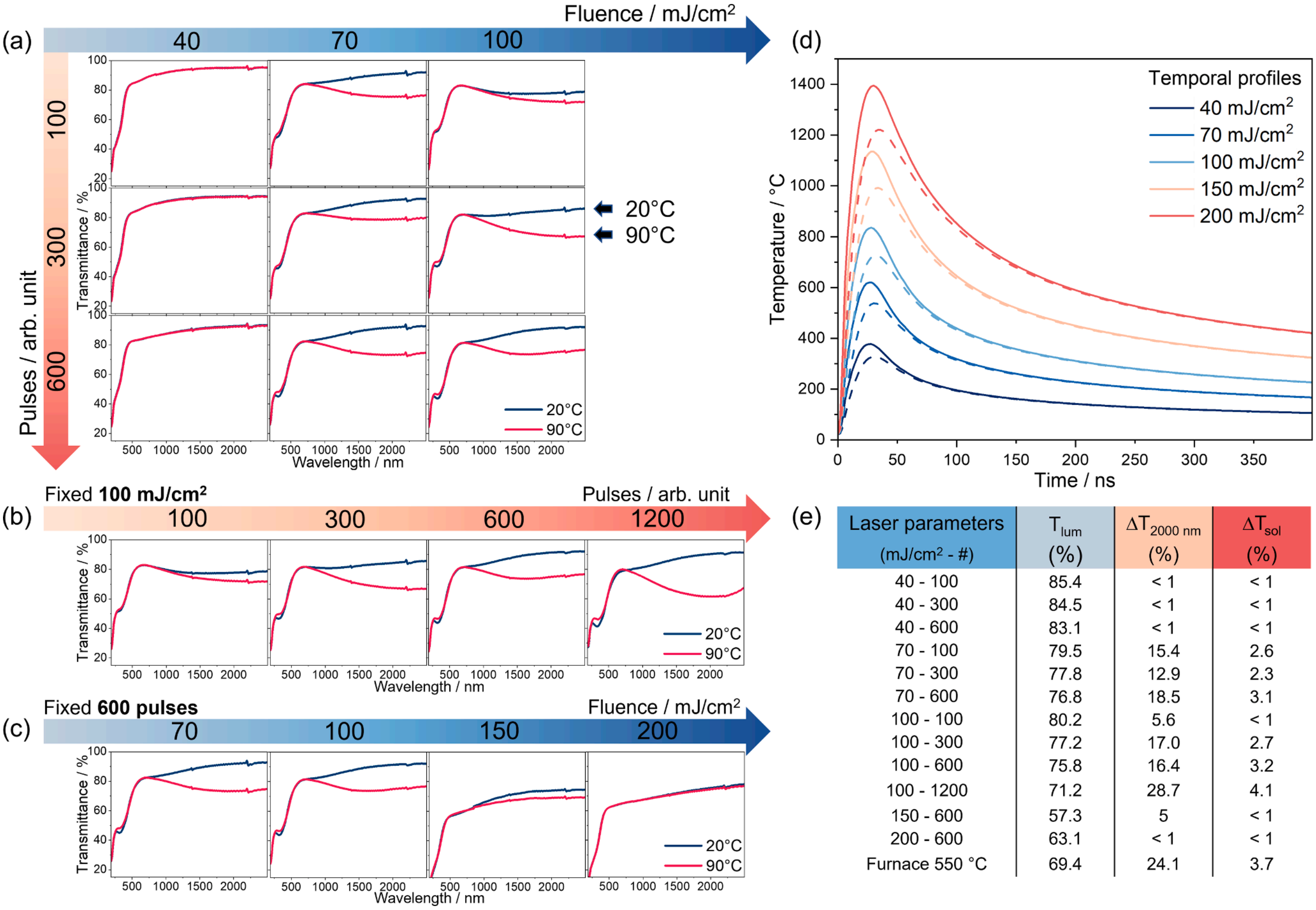

Laser parameters (mJ/cm² - #)	T_{lum} (%)	$\Delta T_{2000\ nm}$ (%)	ΔT_{sol} (%)
40 - 100	85.4	< 1	< 1
40 - 300	84.5	< 1	< 1
40 - 600	83.1	< 1	< 1
70 - 100	79.5	15.4	2.6
70 - 300	77.8	12.9	2.3
70 - 600	76.8	18.5	3.1
100 - 100	80.2	5.6	< 1
100 - 300	77.2	17.0	2.7
100 - 600	75.8	16.4	3.2
100 - 1200	71.2	28.7	4.1
150 - 600	57.3	5	< 1
200 - 600	63.1	< 1	< 1
Furnace 550 °C	69.4	24.1	3.7

Fig. 6. (a) Transmittance at 20°C and 90°C of the laser-annealed spots on the fused silica substrates, at increasing values of fluence (40–100 mJ/cm^2) and pulse number (100–600), respectively. (b) Transmittance at 20°C and 90°C of the laser-annealed spots at fixed fluence of 100 mJ/cm^2 and increasing values of pulse number (100–1200). (c) Transmittance at 20°C and 90°C of the laser-annealed spots at fixed pulse number of 600 and increasing values of fluence (70–200 mJ/cm^2). All the spectra are related to the 33 ± 5 nm lasered thin films. (d) Simulations of the temperature profiles over time throughout the films on fused silica substrates, during a single pulse of laser irradiation, at increasing fluence between 40 and 200 mJ/cm^2. For each fluence, the temperature was simulated at the film's surface (solid line) and at the interface between the film and the substrate (dashed line). (e) Thermochromic efficiency values of the lasered spots and of the reference furnace annealed film on the fused silica substrates, including the luminous transmittance (T_{lum}), the transmittance modulation efficiency at 2000 nm ($\Delta T_{2000\ nm}$) and the solar modulation efficiency (ΔT_{sol}).

temporal evolution of the temperature was simulated both at the film surface and at the substrate interface (Fig. 6 (d)). The maximum surface temperature was reached between 22 and 25 ns for all the fluences (40–200 mJ/cm^2). A single pulse at 40 mJ/cm^2 increased the surface temperature to a maximum peak of ~380°C, while fluences of 70–100 mJ/cm^2 led to peak temperatures of ~620-840°C. The simulated temperatures were close or above to the crystallization range during conventional heating, which is usually located at 400–600°C [23,37]. Considering the depth profiles (Fig. S9 in SI), simulated for single pulses at 40, 70, and 100 mJ/cm^2 at increasing irradiation time, the temperature increase involved all the film thickness and propagated into the first few hundreds of nm of the substrate. After 22 ns, a 100 mJ/cm^2 fluence led to a peak surface temperature of ~840°C (Fig. S9 (c) in SI). At the same timescale, the temperature experience at 500 nm depth from the surface was ~300°C (Fig. S9 (d) in SI). The depth profiles confirmed the heat confinement allowed by laser annealing, which minimizes the thermal damage of the substrate respect to conventional furnace treatment.

According to recent literature, a proposed explanation regarding the amorphous-to-crystalline conversion during laser annealing is related to the effective annealing time (t_{eff}) [69]. The latter is defined as the time over which the temperature experienced by the film exceeds the heat-induced crystallization temperature. The t_{eff} was found to be less than a hundred ns in several compounds. This can explain the successful crystallization of the films even within a minute of laser irradiation, since 600 pulses at 10 Hz frequency correspond to 1 min. The simulations can only describe the temperature distribution and teff during a single pulse, therefore the influence of increasing pulse number was not accounted. The physical parameters used in the simulations were chosen according to the literature, which offers a broad range of values in function of the fabrication technique [70], whereas the optical absorption was calculated from ellipsometry data (see Experimental section). Due to the nature of sol–gel process, the increasing number of pulses determines an evolution of the film in terms of morphological, physical, and thermal properties, which in turn influence the real temperatures experienced throughout the film. Nonetheless, the simulations offer a useful estimation of the temperature distribution during the pulsed irradiation, since the simulated temperatures match with our experimental results.

Following the identification of the crystallization threshold on fused silica substrates, the fluence was further increased to verify the eventual presence of an upper threshold (Fig. 6 (c-e)). The increase of fluence to 150 mJ/cm^2 led to a decrease of the transmittance modulation ($\Delta T_{2000\ nm}$ = 5%), which almost disappeared at 200 mJ/cm^2 ($\Delta T_{2000\ nm} \sim 0\%$).

To explain the gradual modulation decrease and disappearance seen after 100 mJ/cm^2, a chemical and morphological analysis were carried by XPS and SEM (Fig. S10 in SI and Fig. 7). The key core levels from XPS showed the same key features as discussed for the silicon substrate

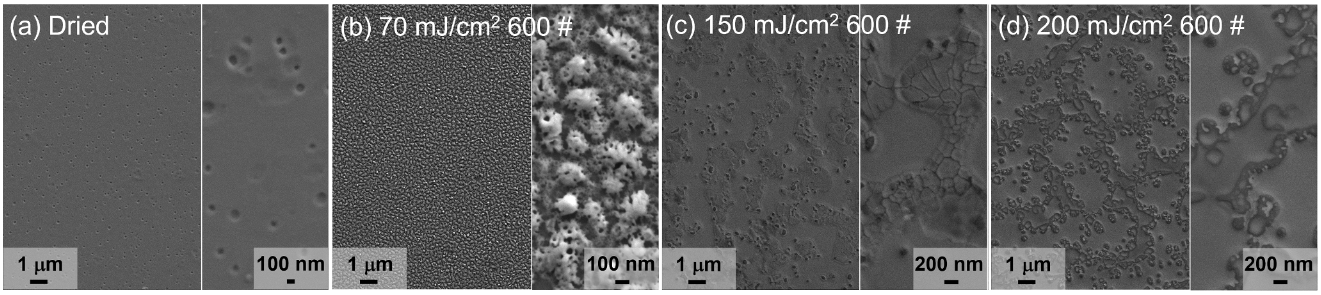

Fig. 7. SEM images of (a) the dried film and (b-d) the lasered spots on the fused silica substrates, including (b) 70 mJ/cm^2 600 #, (c) 150 mJ/cm^2 600 #, (d) 200 mJ/cm^2 600 #. The relative scale bars are inserted at the bottom of each image.

(Fig. S10 in the SI). A higher V^{5+}/V^{4+} ratio was detected on the samples which showed a degradation in the optical modulation (i.e., 150–200 mJ/cm^2). From the SEM analysis, before laser curing the dried sample displayed a smooth and uniform morphology, in analogy with the silicon substrate (Fig. 7 (a) and Fig. S6 (a)). While 600 # at 70 mJ/cm^2 led to the formation of similar nanofeatures as found for the silicon substrate, the samples cured at the two highest fluences (150–200 mJ/cm^2) displayed different morphologies. At 150 mJ/cm^2, molten-like islands were formed on the sample's surface. An increase of fluence to 200 mJ/cm^2 determined the extension of the molten area, which covered most of the surface and caused the degradation of solar modulation.

From the simulations (Fig. 6 (d)), single pulses at 150–200 mJ/cm^2 determined increases in temperature up to ~1100-1400°C in a nanosecond timescale, respectively. The melting of bulk VO_2 happens at ~1500°C [71], even though several studies on VO_2 thin film found that melting could occur below 1000°C [72]. The smooth interconnected island morphologies in Fig. 7 (c-d) could be related to the partial melting of the film's surface, since the heat distribution during laser irradiation follows a non-equilibrium process, happening over an extremely fast timescale respect to conventional furnace heating. As shown before, the surface is covered by a thin oxidized layer, which could have additionally helped the non-equilibrium melting due to its lower melting temperature of ~690°C [71]. Similar superficial melted morphologies were found when threshold laser fluences were reached on both sputtered crystalline V_2O_5 films [73] and on amorphous sol gel ZnO films [74], in which the melting threshold was found to be higher on silicon substrates respect to polyimide. To verify the influence of the substrate, the increase of the fluence above 100 mJ/cm^2 was done on the silicon substrate as well. On the latter, the molten morphology was reached with a 300 mJ/cm^2 fluence (Fig. S11 in SI). The higher fluence required to reach the melted morphologies on silicon can be explained by the higher thermal diffusivity respect to fused silica, as well as the higher light absorption at 248 nm. The latter may have led to lower temperatures inside the film at the same fluence and lower exposure time to the photogenerated heat.

5. Conclusion

VO_2 thin films, obtained via a green sol–gel process, were crystallized by pulsed excimer laser annealing and the effect of laser fluence and pulse number was separately studied. Threshold laser parameters to aid the VO_2 crystallization and avoid the surface melting were found. The VO_2 crystallization was achieved within only 60 s of laser exposure, performed at room temperature in air, after a 10 min drying step at 300°C. The temperature profile simulations confirmed the heat confinement within the film during the laser pulses, with negligible substrate heating. The thermochromic properties of the lasered thin films ($T_{lum} = 71.2\%$, $\Delta T_{2000\ nm} = 28.7\%$, $\Delta T_{sol} = 4.1\%$) displayed a high T_{lum} and were comparable with both the reference furnace-treated films and with other single-layer VO_2 thin films in literature. Further increase in ΔT_{sol}, without compromising the T_{lum}, could be obtained by combining VO_2 with other materials in multilayer configurations. The thin film crystallization by pulsed laser annealing opens multiple possibilities to exploit the MIT of VO_2 for several applications, from smart windows to flexible electronics to metamaterials.

CRediT authorship contribution statement

Maria Basso: Conceptualization, Methodology, Validation, Investigation, Data curation, Writing – original draft, Visualization. **Elena Colusso:** Conceptualization, Investigation, Data curation, Funding acquisition. **Chiara Carraro:** Investigation. **Curran Kalha:** Investigation, Methodology. **Aysha A. Riaz:** Investigation. **Giada Bombardelli:** Investigation. **Enrico Napolitani:** Writing – review & editing, Supervision, Project administration, Funding acquisition. **Yu Chen:** Investigation. **Jacek Jasieniak:** Supervision, Project administration, Funding acquisition. **Laura E. Ratcliff:** Software, Formal analysis. **Pardeep K. Thakur:** Investigation. **Tien-Lin Lee:** Investigation. **Anna Regoutz:** Writing – review & editing, Supervision, Project administration, Funding acquisition. **Alessandro Martucci:** Conceptualization, Writing – review & editing, Supervision, Project administration, Funding acquisition.

Declaration of Competing Interest

The authors declare the following financial interests/personal relationships which may be considered as potential competing interests: [Alessandro Martucci reports financial support was provided by University of Padova.]

Data availability

Data will be made available on request.

Acknowledgement

MB acknowledges Gini Foundation and CARIPARO foundation for financial support. EN and AM acknowledge UNIPD for financial support (grant UNIPD-ISR 2017 'SENSITISE'). EC and AM acknowledge funding through the SID project (BIRD221997) under the BIRD 2022 program sponsored by the University of Padua. JJ acknowledges financially by the Australia Research Council funded Centre of Excellence in Exciton Science (Grant CE170100026). The authors acknowledge the use of the instruments at the Monash Centre for Electron Microscopy (MCEM), a Node of Microscopy Australia. AM and JJ thanks University of Padova and Monash University for financial support through the joint initiatives in education and research program. AR acknowledges the support from the Analytical Chemistry Trust fund for her CAMS-UK fellowship. CK and AAR acknowledge the support from the Department of Chemistry, UCL. This work was carried out with support of Diamond Light Source, instrument I09 (proposal NT29451-4). The authors would like to thank Dave McCue, I09 beamline technician, for his support of the

experiments.

Appendix A. Supplementary material

The Supplementary Information is available, including additional SXPS and HAXPES data, DFT calculations, ellipsometry data, UV-Vis-NIR transmittance data, SEM images, temperature profile simulations. Supplementary data to this article can be found online at https://doi.org/10.1016/j.apsusc.2023.157507.

References

[1] X. Cao, T. Chang, Z. Shao, F. Xu, H. Luo, P. Jin, Challenges and opportunities toward real application of VO_2-based smart glazing, Matter 2 (2020) 862–881.

[2] M.M. Seyfouri, R. Binions, Sol-gel approaches to thermochromic vanadium dioxide coating for smart glazing application, Sol. Energy Mater. Sol. Cells 159 (2017) 52–65.

[3] J. Leroy, A. Bessaudou, F. Cosset, A. Crunteanu, Structural, electrical and optical properties of thermochromic VO 2 thin films obtained by reactive electron beam evaporation, Thin Solid Films 520 (2012) 4823–4825.

[4] K. Liu, S. Lee, S. Yang, O. Delaire, J. Wu, Recent progresses on physics and applications of vanadium dioxide. 2018.

[5] A. Sood, X. Shen, Y. Shi, S. Kumar, S.J. Park, M. Zajac, Y. Sun, L.Q. Chen, S. Ramanathan, X. Wang, W.C. Chueh, A.M. Lindenberg, Universal phase dynamics in VO_2 switches revealed by ultrafast operando diffraction, Science 373 (2021) 352–355.

[6] S. Wang, M. Liu, L. Kong, Y. Long, X. Jiang, A. Yu, Recent progress in VO_2 smart coatings: Strategies to improve the thermochromic properties, Prog. Mater Sci. 81 (2016) 1–54.

[7] S.A. Howard, E. Evlyukhin, G. Páez Fajardo, H. Paik, D.G. Schlom, L.F. Piper, Digital Tuning of the transition temperature of epitaxial VO_2 thin films on MgF2 substrates by strain engineering, Adv. Mater. Interfaces 8 (2021) 2001790.

[8] S. Wall, S. Yang, L. Vidas, M. Chollet, J.M. Glownia, M. Kozina, T. Katayama, T. Henighan, M. Jiang, T.A. Miller, D.A. Reis, L.A. Boatner, O. Delaire, M. Trigo, Ultrafast disordering of vanadium dimers in photoexcited VO_2, Science 362 (2018) 572–576.

[9] D. Wegkamp, M. Herzog, L. Xian, M. Gatti, P. Cudazzo, C.L. McGahan, R.E. Marvel, R.F. Haglund, A. Rubio, M. Wolf, J. Stähler, Instantaneous band gap collapse in photoexcited monoclinic VO_2 due to photocarrier doping, Phys. Rev. Lett. 113 (2014), 216401.

[10] R. Sun, B. Jin, L. Yao, Y. Liu, J. Li, J. Liang, J. He, Controllable design of bifunctional VO_2 coatings with superhydrophobic and thermochromic performances, ACS Appl. Mater. Interfaces 13 (2021) 13751–13759.

[11] Y. Li, H. Ma, F. Tang, C. Li, B. Wang, X. Song, K. Liu, X. Zhang, Direct laser writing of multishaped VO_2 microactuators based on freestanding VO_2 film, Advanced Materials Technologies 8 (2023) 2200977.

[12] E. Yarali, C. Koutsiaki, H. Faber, K. Tetzner, E. Yengel, P. Patsalas, N. Kalfagiannis, D.C. Koutsogeorgis, T.D. Anthopoulos, Recent progress in photonic processing of metal-oxide transistors, Adv. Funct. Mater. 30 (2020) 1–37.

[13] G. Tan, J.-H. Lee, Y.-H. Lan, M.-K. Wei, L.-H. Peng, I.-C. Cheng, S.-T. Wu, Broadband antireflection film with moth-eye-like structure for flexible display applications, Optica 4 (2017) 678.

[14] N.M. Twyman, K. Tetzner, T.D. Anthopoulos, D.J. Payne, A. Regoutz, Rapid photonic curing of solution-processed In 2O3 layers on flexible substrates, Appl. Surf. Sci. 479 (2019) 974–979.

[15] E. Carlos, E. Carlos, S. Dellis, N. Kalfagiannis, L. Koutsokeras, D.C. Koutsogeorgis, R. Branquinho, R. Martins, E. Fortunato, Laser induced ultrafast combustion synthesis of solution-based AlO: Xfor thin film transistors, J. Mater. Chem. C 8 (2020) 6176–6184.

[16] P.Y. Chang, et al., Near-infrared laser-annealed IZO flexible device as a sensitive H2S sensor at room temperature, ACS Appl. Mater. Interfaces 12 (2020) 24984–24991.

[17] D. Pérez-Mezcua, I. Bretos, R. Jiménez, J. Ricote, R.J. Jiménez-Rioboó, C.G. Da Silva, D. Chateigner, L. Fuentes-Cobas, R. Sirera, M.L. Calzada, Photochemical solution processing of films of metastable phases for flexible devices: the β -Bi2O3 polymorph, Sci. Rep. 6 (2016) 1–10.

[18] Y.R. Jo, W.J. Lee, M.H. Yoon, B.J. Kim, In situ tracking of low-temperature VO_2 crystallization via photocombustion and characterization of phase-transition reliability on large-area flexible substrates, Chem. Mater. 32 (2020) 4013–4023.

[19] M. Nishikawa, T. Nakajima, T. Kumagai, T. Okutani, T. Tsuchiya, Ti-doped VO_2 films grown on glass substrates by excimer-laser-assisted metal organic deposition process, Jpn. J. Appl. Phys. 50 (2011).

[20] E. Breckenfeld, H. Kim, E.P. Gorzkowski, T.E. Sutto, A. Piqué, Laser-processing of VO2 thin films synthesized by polymer-assisted-deposition, Appl. Surf. Sci. 397 (2017) 152–158.

[21] R. Molaei, R. Bayati, S. Nori, D. Kumar, J.T. Prater, J. Narayan, Diamagnetic to ferromagnetic switching in VO_2 epitaxial thin films by nanosecond excimer laser treatment, Appl. Phys. Lett. 103 (2013), 252109.

[22] L. Li-Bin, L. Tie-Cheng, L. Yong, L. Qiang, Variation of morphology and color of VO_2 thin films induced by excimer laser, Nucl. Instrum. Methods Phys. Res., Sect. B 191 (2002) 102–105.

[23] M. Pan, H. Zhong, S. Wang, J. Liu, Z. Li, X. Chen, W. Lu, Properties of VO_2 thin film prepared with precursor VO(acac)2, J. Cryst. Growth 265 (2004) 121–126.

[24] T. Chang, X. Cao, Y. Long, H. Luo, P. Jin, How to properly evaluate and compare the thermochromic performance of VO_2-based smart coatings, J. Mater. Chem. A 7 (2019) 24164–24172.

[25] S. Tanuma, C.J. Powell, D.R. Penn, Calculations of electron inelastic mean free paths. V. Data for 14 organic compounds over the 50–2000 eV range, Surf. Interface Anal. 21 (1994) 165–176.

[26] D.E. Hoglund, M.O. Thompson, Experimental test of morphological stability theory for a planar interface during rapid solidification, Phys. Rev. B - Condensed Matter Mater. Phys. 58 (1998) 189–199.

[27] H. Kizuka, T. Yagi, J. Jia, Y. Yamashita, S. Nakamura, N. Taketoshi, Y. Shigesato, Temperature dependence of thermal conductivity of VO_2 thin films across metal-insulator transition, Jpn. J. Appl. Phys. 54 (2015), 053201.

[28] Y.S. Touloukian, R.W. Powell, C.Y. Ho, P. Klemens, Thermophysical properties of matter-, Thermal Cond.: Nonmetallic Solids (1970).

[29] P. Hohenberg, W. Kohn, Inhomogeneous electron gas, Phys. Rev. 136 (1964) B864.

[30] W. Kohn, L.J. Sham, Self-consistent equations including exchange and correlation effects, Phys. Rev. 140 (1965) A1133.

[31] S.J. Clark, M.D. Segall, C.J. Pickard, P.J. Hasnip, M.I. Probert, K. Refson, M. C. Payne, First principles methods using CASTEP, Z. Kristallogr. 220 (2005) 567–570.

[32] J.P. Perdew, K. Burke, M. Ernzerhof, Generalized gradient approximation made simple, Phys. Rev. Lett. 77 (1996) 3865.

[33] H.J. Monkhorst, J.D. Pack, Special points for Brillouin-zone integrations, Phys. Rev. B 13 (1976) 5188.

[34] A. Tkatchenko, M. Scheffler, Accurate molecular van der Waals interactions from ground-state electron density and free-atom reference data, Phys. Rev. Lett. 102 (2009), 073005.

[35] H. Palneedi, J.H. Park, D. Maurya, M. Peddigari, G.T. Hwang, V. Annapureddy, J. W. Kim, J.J. Choi, B.D. Hahn, S. Priya, K.J. Lee, J. Ryu, Laser irradiation of metal oxide films and nanostructures: applications and advances, Adv. Mater. 30 (2018) 1–38.

[36] D.D.W. Green, D.M.Z. Southard, Perry's Chemical Engineers' Handbook, McGraw-Hill Education (2019) 1354–1383.

[37] Z. Zhang, Y. Gao, Z. Chen, J. Du, C. Cao, L. Kang, H. Luo, Thermochromic VO_2 thin films: Solution-based processing, improved optical properties, and lowered phase transformation temperature, Langmuir 26 (2010) 10738–10744.

[38] P.C. With, J. Lehnert, L. Seifert, S. Dietrich, H. Krautscheid, S. Naumov, A. Prager, B. Abel, L. Prager, U. Helmstedt, Photochemical low-temperature synthesis of iron (III) oxide thin films, Appl. Surf. Sci. 493 (2019) 525–532.

[39] A. Samotus, R. Grybos, N. Popova, K. Bogolitsyn, Kinetics of oxidation of vanadyl acetylacetonate by oxygen in methanolic solution. 64 (1997) 2–5.

[40] T.P. Melia, R. Merrifield, Thermal properties of acetylacetone, J. Appl. Chem. 19 (2007) 79–82.

[41] J. Von Hoene, R.G. Charles, W.M. Hickam, Thermal decomposition of metal acetylacetonates mass spectrometer studies, J. Phys. Chem. 62 (1958) 1098–1101.

[42] R.N. Nenashev, N.E. Mordvinova, V.P. Zlomanov, V.L. Kuznetsov, Thermal decomposition of vanadyl acetylacetonate, Inorg. Mater. 51 (2015) 891–896.

[43] Y.H. Kim, J.S. Heo, T.H. Kim, S. Park, M.H. Yoon, J. Kim, M.S. Oh, G.R. Yi, Y. Y. Noh, S.K. Park, Flexible metal-oxide devices made by room-temperature photochemical activation of solgˆ C“gel films, Nature 489 (2012) 128–132.

[44] P.C. With, U. Helmstedt, L. Prager, Flexible transparent barrier applications of oxide thin films prepared by photochemical conversion at low temperature and ambient pressure, Front. Mater. (2020) 7.

[45] C.S. Sandu, V.S. Teodorescu, C. Ghica, B. Canut, M.G. Blanchin, J.A. Roger, A. Brioude, T. Bret, P. Hoffmann, C. Garapon, Densification and crystallization of SnO 2: Sb sol-gel films using excimer laser annealing, Appl. Surf. Sci. 208–209 (2003) 382–387.

[46] C.Y. Tsay, M.C. Wang, Structural and optical studies on sol-gel derived ZnO thin films by excimer laser annealing, Ceram. Int. 39 (2013) 469–474.

[47] M. Nishikawa, T. Nakajima, T. Manabe, T. Okutani, T. Tsuchiya, High temperature coefficients of resistance of VO_2 films grown by excimer-laser-assisted metal organic deposition process for bolometer application, Mater. Lett. 64 (2010) 1921–1924.

[48] J.C. Dupin, D. Gonbeau, P. Vinatier, A. Levasseur, Systematic XPS studies of metal oxides, hydroxides and peroxides, PCCP 2 (2000) 1319–1324.

[49] M. Çopurogìlu, H. Sezen, R.L. Opila, S. Suzer, Band-bending at buried SiO2/Si interface as probed by XPS, ACS Appl. Mater. Interfaces 5 (2013) 5875–5881.

[50] P.C. With, U. Helmstedt, S. Naumov, A. Sobottka, A. Prager, U. Decker, R. Heller, B. Abel, L. Prager, Low-Temperature photochemical conversion of organometallic precursor layers to titanium(IV) oxide thin films, Chem. Mater. 28 (2016) 7715–7724.

[51] H. Kim, Y. Kim, K.S. Kim, H.Y. Jeong, A.R. Jang, S.H. Han, D.H. Yoon, K.S. Suh, H. S. Shin, T. Kim, W.S. Yang, Flexible thermochromic window based on hybridized VO_2/graphene, ACS Nano 7 (2013) 5769–5776.

[52] J. Zhang, Z. Zhao, J. Li, H. Jin, F. Rehman, P. Chen, Y. Jiang, C. Chen, M. Cao, Y. Zhao, Evolution of structural and electrical properties of oxygen-deficient VO_2 under low temperature heating process, ACS Appl. Mater. Interfaces 9 (2017) 32.

[53] G. Silversmit, D. Depla, H. Poelman, G.B. Marin, R. De Gryse, Determination of the V2p XPS binding energies for different vanadium oxidation states (V5+ to V0+), J. Electron Spectrosc. Relat. Phenom. 135 (2004) 167–175.

[54] G. Bordelet, I. Yamaguchi, T. Manabe, T. Tsuchiya, Low temperature vanadium oxide thin film sintering by thermal and excimer-laser-assisted Metal-Organic Deposition (MOD), Ceram. Int. 44 (2018) S26–S29.

[55] R. Lopez, L.A. Boatner, T.E. Haynes, Synthesis and characterization of size-controlled vanadium dioxide nanocrystals in a fused silica matrix, J. Appl. Phys. 92 (2002) 4031.

[56] T. Tsuchiya, T. Nakajima, Y.U.C. European, Flexible and Epitaxial Metal Oxide Thin Film Growth by Photoreaction Processing for Electrical and Optical Applications. Wiley Online Library 2020, pp. 9261–9276.

[57] T.H. Im, J.H. Lee, H.S. Wang, S.H. Sung, Y.B. Kim, Y. Rho, C.P. Grigoropoulos, J. H. Park, K.J. Lee, Flashlight-material interaction for wearable and flexible electronics, Mater. Today 51 (2021) 525–551.

[58] K.D. Rogers, An X-ray diffraction study of semiconductor and metallic vanadium dioxide, Powder Diffr. 8 (1993) 240–244.

[59] T. Paik, S.H. Hong, E.A. Gaulding, H. Caglayan, T.R. Gordon, N. Engheta, C. R. Kagan, C.B. Murray, Solution-processed phase-change VO_2 metamaterials from colloidal vanadium oxide (VOx) nanocrystals, ACS Nano 8 (2014) 797–806.

[60] L. Yao, Z. Qu, R. Sun, Z. Pang, Y. Wang, B. Jin, J. He, Long-lived multilayer coatings for smart windows: integration of energy-saving, antifogging, and self-healing functions, ACS Appl. Energy Mater. 2 (2019) 7467–7473.

[61] C. Zhang, Q. Yang, C. Koughia, F. Ye, M. Sanayei, S.J. Wen, S. Kasap, Characterization of vanadium oxide thin films with different stoichiometry using Raman spectroscopy, Thin Solid Films 620 (2016) 64–69.

[62] T. Kallel, M. Dammak, J. Wang, W.M. Jadwisienczak, Raman characterization and stress analysis of AlN: Er 3+ epilayers grown on sapphire and silicon substrates, Mater. Sci. Eng. B 187 (2014) 46–52.

[63] N.F. Quackenbush, State University of New York at Binghamton. Department of Physics, A. P.; Astronomy. The physics of ultra-thin vanadium dioxide: At the surface, interface and in-between. PhDT 2016.

[64] Y.X. Ji, S.Y. Li, G.A. Niklasson, C.G. Granqvist, Durability of thermochromic VO_2 thin films under heating and humidity: Effect of Al oxide top coatings, Thin Solid Films 562 (2014) 568–573.

[65] R.J. Winfield, L.H. Koh, S. O'Brien, G.M. Crean, Excimer laser processing of ZnO thin films prepared by the sol-gel process, Appl. Surf. Sci. 254 (2007) 855–858.

[66] Y.F. Joya, Z. Liu, Effect of the excimer laser irradiation on sol-gel derived tungsten-titanium dioxide thin films, Appl. Phys. A 102 (2011) 91–97.

[67] J. Wu, W. Huang, Q. Shi, J. Cai, D. Zhao, Y. Zhang, J. Yan, Effect of annealing temperature on thermochromic properties of vanadium dioxide thin films deposited by organic sol-gel method, Appl. Surf. Sci. 268 (2013) 556–560.

[68] J.H. Yu, S.H. Nam, D. Kim, M. Kim, H.J. Seo, Y.H. Ro, Y.T. Joo, J. Lee, J.H. Boo, Thermal aging effect of vanadyl acetylacetonate precursor for deposition of VO_2 thin films with thermochromic properties, Mater. Res. Bull. 82 (2016) 11–15.

[69] Y. Matsubayashi, J. Nomoto, I. Yamaguchi, T. Tsuchiya, Control of the oxygen deficiency and work function of SrFeO3-: δ thin films by excimer laser-assisted metal organic decomposition, CrstEngComm 22 (2020) 4685–4691.

[70] M. Currie, M.A. Mastro, V.D. Wheeler, M.K. Davis, M.J.F. Digonnet, Characterizing the tunable refractive index of vanadium dioxide, Optical Mater. Express 7 (2017) 1697–1707.

[71] W. Haynes, D. Lide, T. Bruno, CRC Handbook of Chemistry and Physics, CRC Press, 2016.

[72] S.S. Maklakov, V.I. Polozov, S.A. Maklakov, A.D. Mishin, I.A. Ryzhikov, A. L. Trigub, V.A. Amelichev, K.I. Maslakov, V.N. Kisel, Post-deposition annealing of thin RF magnetron sputter-deposited VO_2 films above the melting point, J. Alloy. Compd. 763 (2018) 558–569.

[73] M. Kang, E. Oh, I. Kim, S.W. Kim, J.W. Ryu, Y.G. Kim, Optical characteristics of amorphous V_2O_5 thin films colored by an excimer laser, Curr. Appl Phys. 12 (2012) 489–493.

[74] G. Fiaschi, S. Mirabella, G. Franzò, L. Maiolo, A. Chitu, Y. Komem, Y. Shacham-Diamand, Effect of laser annealing on ZnO nanorods grown by chemical bath deposition on flexible substrate, Appl. Surf. Sci. 458 (2018) 800–804.